Hindawi
International Journal of Photoenergy
Volume 2019, Article ID 4981631, 15 pages
https://doi.org/10.1155/2019/4981631

Research Article

Photo-Fenton Degradation of RB5 Dye in Aqueous Solution Using Fe Supported on Mexican Natural Zeolite

José Domenzain-Gonzalez,[1] **José J. Castro-Arellano**,[1] **Luis A. Galicia-Luna**,[1] **and Luis Lartundo-Rojas**[2]

[1]*Instituto Politécnico Nacional, ESIQIE, Laboratorio de Termodinámica, Sección de Estudios de Posgrado e Investigación, UPALM, 07738 CDMX, Mexico*
[2]*Instituto Politécnico Nacional, Centro de Nanociencias y Micro y Nanotecnologías, UPALM, 07738 CDMX, Mexico*

Correspondence should be addressed to José J. Castro-Arellano; jjcastroarellano@gmail.com
and Luis A. Galicia-Luna; lagalicialuna@gmail.com

Received 4 June 2019; Revised 24 August 2019; Accepted 12 October 2019; Published 21 November 2019

Academic Editor: Leonardo Palmisano

A Mexican natural zeolite (MNZ) was impregnated with Fe at concentrations of 5 and 10 mg $FeCl_3$/g MNZ (MNZ/Fe) in order to study the photo-Fenton degradation of Reactive Black 5 (RB5) dye. Two samples were prepared and calcined at 550 and 700°C for each concentration. These samples were also characterized by the following techniques: X-ray diffraction (XRD) to determine crystalline phases of mineral, X-ray photoelectron spectroscopy (XPS) to observe the elemental composition of the material where the main element was Fe as Fe2p, Mössbauer to establish the phases in the material which were magnetite (Fe_3O_4), fayalite, and chlorite, Raman to corroborate that magnetite clusters in natural material were presented, and transmission electron microscopy (TEM) by which magnetite nanoparticles were observe on zeolite surface. Afterwards, the catalytic degradation of RB5 dye was performed by photo-Fenton process using a 2.2 W lamp as a radiation source. Four initial concentrations of RB5 dye ($(RB5)_0$) were evaluated which ranged from 40 to 100 mg/L. Then, the evaluation reaction was carried out by UV-Vis spectroscopy to know the change in RB5 concentration and chemical oxygen demand (COD) removal to determine the organic carbon. The best results on the photo-Fenton degradation was 91% discoloration and 68.5% chemical oxygen demand removal based on an initial concentration $(RB5)_0 = 100$ mg/L and 10 mg MNZ/Fe (700°C of calcined temperature) at (MNZ/Fe) = 0.05 g/L catalyst dose in aqueous solution, $(H_2O_2) = 3$ g/L, pH = 2.5, and 180 minutes of reaction time. Subsequently, variations on $(RB5)_0$, pH, (H_2O_2), and (MNZ/Fe) were assessed in order to optimize the process by keeping 10 MNZ/Fe. The optimal RB5 dye degradation was achieved at $(RB5)_0 = 100$ mg/L in the presence of (MNZ/Fe) = 0.2 g/L, $(H_2O_2) = 3$ g/L and pH = 2.5 where the highest discoloration and chemical oxygen demand removal were 93 and 70.5 at 180 min. Finally, the kinetic reaction was evaluated as a pseudo-first-order kinetics with an apparent rate constant (k_{app}) of 0.0225 min^{-1} at latest conditions.

1. Introduction

Nowadays, the environment pollution is increasing due to the different human activities. The high content of harmful organic and inorganic compounds present in rivers, lakes, and seas represents an unfavorable impact for life development in these ecosystems, in addition to having a pernicious influence on humanity. There are a great variety of pollution sources, which are produced by human activities that affect the soil, air, and liquid effluents. The chemical industry has the greatest impact on pollution increase, since it throws liquid effluents and/or gases with chemical waste to the environment. Some organic pollutant species are resistant to natural degradation process [1, 2]. A notorious example is the textile industry, which often throws wastewater effluents with nonbiodegradable dyes to the environment [3]. In consequence, the development of new processes or materials is needed for the elimination of these compounds based on

natural materials. An alternative is the Fenton process which allows obtaining a high efficiency over the effluent treatments and even reaching mineralization in the presence of Fe as a catalyst. Then, a natural zeolite can be used as support and/or promoter since it is constituted by Fe and other metals.

The zeolites can be classified as natural or synthetic. Synthetic zeolites have a homogeneous composition, a specific structure, and well-defined properties that depend on the control of the synthesis process. These characteristics allow their application in selective high-performance reactions and are widely used in the industry, but they have a higher cost than natural zeolites. Moreover, natural zeolites have a heterogeneous composition, their structure and properties can vary from one lot to another, and even change their properties and composition in the same sample according to the crystal or the analyzed zone. Despite natural zeolites being not very selective, they are reactive, more abundant, and crystalline aluminosilicates with ion exchange capacity. The latter allows the adsorption of minerals such as K, Na, C, Ca, Mg, and Fe, and hence its application in several chemical reactions. To resume, natural zeolites are a good option as catalysts or catalytic supports where selectivity is not as important as the degradation of organic pollutants in wastewater treatment [4, 5].

Zeolites without heterogeneous atoms into its lattice are not photocatalytically active since they do not exhibit any absorption in the UV-Vis region [6], but MNZ has different elements integrated in its composition as Fe that produces photoactive sites of a solid photocatalyst. Besides, the great surface area of MNZ is combined with the absorption capacity and ion exchange provided by its negative charge [7]. It causes an increase in photocatalytic process efficiency. For this reason, it is interesting to increase the amount of Fe in MNZ. Certain ceramics such as zeolites tend to modify their structural properties (porosity, mechanical strength, composition, chemical properties, among other properties) due to calcination processes.

Fe is a very useful material in several processes, for example, ammonia production [8] or in organic pollutants degradation [9, 10]. Natural minerals constituted of Fe such as hematite and magnetite, among other compounds [11], which are oxides, oxyhydroxides, and hydrated oxides. Goethite is the most frequent iron species in minerals due it being the most thermodynamically stable compound. The presence of these minerals is related to temperature, humidity, and presence of organic matter of soil origin. For example, hematite is associated with warm regions [12], low temperatures, and high humidity, but high contents of organic matter promote goethite formation [13].

An important improvement to the abovementioned process could be Fe nanoparticles, which have many applications in biomedical sciences, removal of heavy metals from aqueous solutions, chemical catalysis, removal of inorganic and organic components, and textile dyes. In the present work, Fe particles were impregnated by incipient wetting method over a Mexican natural zeolite as support with the aim of increasing the Fe concentration. The zeolite impregnated with 5 and 10 mg $FeCl_3$/g MNZ (MNZ/Fe) was used in the RB5 dye degradation by heterogeneous photo-Fenton process. Furthermore, the influence of calcination temperature was determined over Fe species on surface and in the matrix of MNZ/Fe. It was characterized by XRD, XPS, TEM, Mössbauer (MS), and Raman spectroscopy. Meanwhile, UV-Vis spectroscopy and COD removal were used to evaluate the MNZ/Fe catalytic activity.

For the catalytic evaluation, calcined temperature and the amount of MNZ/Fe were evaluated at constant H_2O_2 concentration, catalyst dose in aqueous solution (MNZ/Fe), pH solution, and initial dye concentration $(RB5)_0$. Later, the process was optimized by keeping the radiation source constant and changing the variables (MNZ/Fe), pH solution, (H_2O_2), and $(RB5)_0$. The evaluation parameters were the discoloration percentage and the COD removal at 180 min. Finally, the apparent rate constant was estimated.

2. Materials and Methods

2.1. Preparation. The Mexican natural zeolite (catalytic Fe support) had particle sizes of 38–212 μm. The methodology for MNZ impregnation was in a wet medium (incipient wetting method), which is described below. A MNZ solution with deionized water was prepared and placed under constant stirring and at pH 3 using HCl (0.5 M, 0.38 in mass fraction provided by Fermont). After 120 min, iron salt ($FeCl_3$, 0.9995 in mass fraction provided by Fermont) was added to the solution at concentrations of 5 and 10 mg $FeCl_3$/g MNZ, pH was adjusted to 3 under stirring by 300 min. Subsequently, the material was filtered off and kept at 50°C to remove humidity, and hence avoid modifications in the zeolite structure.

Then, the material was subjected to a calcination process (Vulcan muffle, model 3-130) by increasing temperature at a rate of 2°C/min, with ramps of 100°C and remaining 120 min in each ramp up to reach the desired calcination temperature for 180 min. The calcination temperatures were 300, 600, and 700°C for DXR characterization. Regarding the influence of Fe impregnation, the temperatures were 550 and 700°C. Finally, the calcined MNZ/Fe sample at 700° C was chosen as the best option for catalytic evaluation in the RB5 dye degradation with a concentration of 10 mg MNZ/Fe.

2.2. Characterization. In order to determine the zeolitic phases and Fe species in the mineral, MNZ/Fe was characterized by the following techniques: X-ray diffraction (Rigaku, model Miniflex 600), X-ray photoelectron spectroscopy (Thermo Fisher Scientific, K-Alpha XPS spectrometer), Mössbauer spectroscopy (Wissel-Electronik spectrometer), Raman spectroscopy (Olimpus equipment, model BX41-HR800), and transmission electron microscopy (JEOL, model JEM-2100).

2.3. Evaluation Process of RB5 Dye Degradation. The catalytic evaluation of MNZ/Fe was carried out by a heterogeneous photo-Fenton reaction for removal of Reactive Black 5 dye (0.55 in mass fraction provided by Sigma-Aldrich). This chemical has three characteristic signals in UV-Vis range at 312, 392, and 597 nm which correspond to naphthalene,

azo group, and chromophore that gives color to the molecule, respectively [14, 15].

The catalytic evaluation of MNZ/Fe was carried out in a 200 mL batch reactor with constant stirring at 0.785 bar and room temperature (25°C). In this process, 10 mg MNZ/Fe was used at calcination temperature of 700°C, and catalyst doses in aqueous solution (MNZ/Fe) of 0.05, 0.1, 0.15, 0.2, 0.35, 0.5, 1.0, and 1.5 g/L. The effect of pH on process at 2.5, 3.0, 3.5, and 4.5 was observed by dossing HCl. The effect of H_2O_2 concentration (0.5 in mass fraction provided by Fermont) was also observed with variations of 2, 3, 4, and 5 g/L. Moreover, four initial concentrations of RB5 dye were tested in the range of 40–100 mg/L. In addition, an UV-LED lamp (designed specifically for the geometry of reactor) functioned as the radiation source. The energy provided throughout the lamp improved production of hydroxyl radicals by Fe^{3+} ions. The LEDs emitted at 405 nm corresponding to 3.06 eV and a power of 2.2 W.

RB5 dye removal reactions using MNZ/Fe as a catalyst by the photo-Fenton process were monitored using a UV-Vis spectrophotometer (Ocean Optics, model Jaz) with a radiation source (Analytical Instrument Systems Inc., DT 1000 CE) and optical fibers (Ocean Optics, QP300-1-SR). The calibration curve of the RB5 dye with UV-Vis spectrophotometer was performed from 10 to 100 mg/L each 10 mg/L. The reported data corresponded to the average of triplicated analyses for each concentration, the R^2 was reported to be 0.9987 for 597 nm.

Finally, the chemical oxygen demand (COD) was determined using the reagents provided by Hanna Instruments in the range of 0-1500 mg/L. 2 mL of the sample were needed for COD quantification, the samples were digested in the presence of dichromate at 150°C for 2 hours (HI reactor 839800-01 by Hanna). Subsequently, the samples were cooled at room temperature and the COD was determined by means of a Hanna photometer (HI 83099).

3. Results and Conclusion

3.1. X-Ray Diffraction. Mineral samples were analyzed by X-ray diffraction in order to observe the effect of calcination temperature on zeolite structure. XRD patterns of uncalcined natural zeolite (25°C) and calcined natural zeolite at 300, 600, and 700°C are shown in Figure 1. The material was identified as a mixture of different zeolitic phases where the main phase was mordenite-heulandite, erionite-cristobalite as a secondary phase, and quartz as an impurity. Below 17° 2theta, no significant signals were found that yield information about the material characterization.

Different signals were grouped from 17° 2theta to 68° 2theta where the most intense signal located at 30.9° 2theta was referred to mordenite (JCPDS: O60239). This highest signal remained for any temperatures (25–700°C); however, the intensity was decreasing above 700°C until mineral disappearance at 900°C [16]. Similar behavior was noted for heulandite (JCPDS: 210131), it disappeared at 600°C due to structure collapses above 500°C [17, 18]. On the opposite, erionite (JCPDS: 39-1379) was constituted in the sample up to 700°C and tends to disappear at 840°C [19], erionite

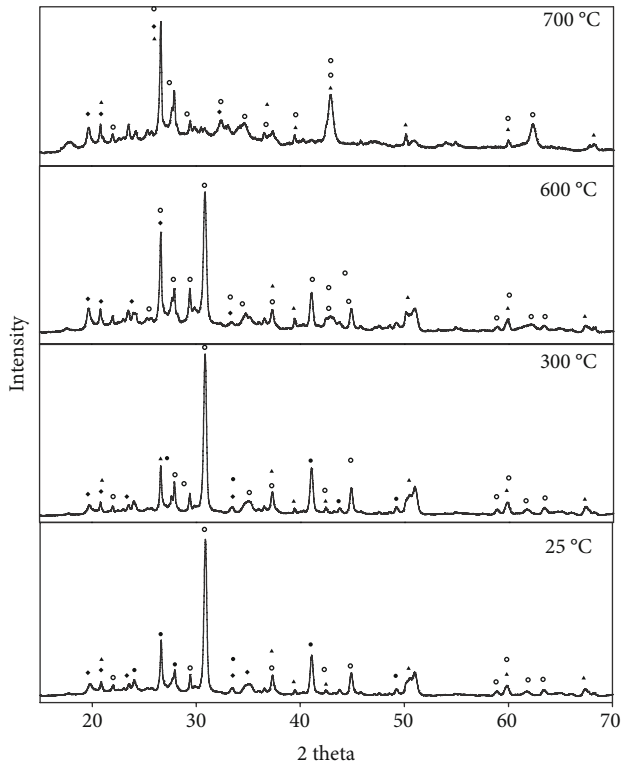

Figure 1: XRD patterns of MNZ/Fe samples for uncalcined at 25°C and calcined at 300, 600, and 700°C: ●: heulandite, ○: mordenite, ✦: erionite, ◇: cristobalite, ▲: quartz.

increased its intensity with respect to the uncalcined sample due to heulandite phase disappears. Besides, as natural zeolite does not have a homogeneous composition, so its structure can change from one sample to another.

Additionally, it is observed that cristobalite (JCPDS: 075-0923) was contained after calcination treatment (up to 700°C) but it disappears at 1525°C [20]. Contrarily, the signals that were located above 55° 2theta corresponded in their great majority to quartz (JCPDS: 46-1045) [21] and mordenite since these phases prevail after calcination at 700°C. Lastly, it was observed that zeolitic structures persisted after the thermal treatment with the exception of heulandite.

3.2. XPS Analysis. X-ray photoelectron spectroscopy analysis gives information about the material surface at a depth not greater than 8 to 10 atomic layers, with a spatial resolution $\leq 6\mu$m. XPS is able to identify the elements from lithium to uranium with exception of hydrogen and helium. The element concentration must be higher than to 0.05% atomic to be detected in the sample [22].

XPS spectra were obtained using a K-alpha X-ray photoelectron spectrometer (Thermo Fisher Scientific Co.) with a monochromatic source of Al Kα X-rays (1486.6 eV). The sample diameter was 400 μm. Firstly, it remained in a prechamber for 600 min; then, samples were transferred to the chamber at about 1×10^{-9} Torr. For each sample, three measurements were carried out in different zones. The analyzer passed energy of 200 eV and 40 eV for the scans collection and high-resolution spectra, respectively. All

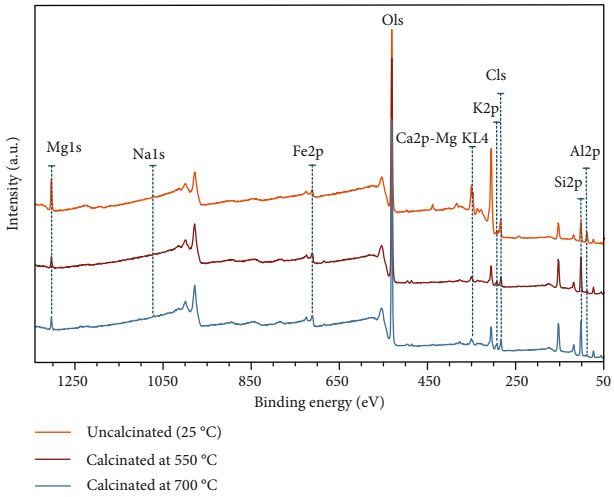

Figure 2: XPS spectra of MNZ/Fe: uncalcined at 25°C and calcined at 550 and 700°C.

Table 1: MNZ composition impregnated with 10 mg $FeCl_3$/g MNZ for calcined and uncalcined samples.

Name	MNZ/Fe composition (w%)		
	(25°C)	(550°C)	(700°C)
O 1 s	47.40	46.00	45.00
Si 2p	27.10	29.00	28.60
Al 2p	8.50	8.40	8.50
Ca 2p	4.10	2.00	2.30
C 1 s	4.00	3.70	4.50
Fe 2p	3.90	6.00	6.20
Mg 1 s	2.20	2.30	2.00
K 2p	1.30	1.30	1.80
Na 1 s	0.80	0.20	0.30

spectra were calibrated with an adventitious peak C1s at 284.6 eV to detect and compensate for the variable charge at core peaks. The software Thermo Avantage v5.979 was used for the curve fitting of a high-resolution spectrum, and the deconvolution was made using the Shirley method with a Gaussian-Lorentzian contribution 70-30%.

Subsequently, Fe species presented in MNZ/Fe were found and identified on the surface. XPS spectra of uncalcined natural zeolite at 25°C as well as calcined at 550 and 700°C are shown in Figure 2. The major elements on surface were Si and Al corroborating an aluminosilicate type material. The amount of Si varied from 27.1 to 29 w% while Al was ranging from 8.4 to 8.5 w%. The presence of Na, Mg, Ca, K, and Fe minerals was also observed.

The global composition of MNZ samples impregnated with 10 mg MNZ/Fe are listed in Table 1 for different temperatures (uncalcined at 25°C and calcined at 550 and 700°C). It can be noted that the composition of Al, C, Mg, K, and Na did not have a significant change. O and Ca composition diminished by comparing calcined and uncalcined analyses. Meanwhile, Si and Fe (3.9 w%) composition increased after the calcination process about 2 percentage

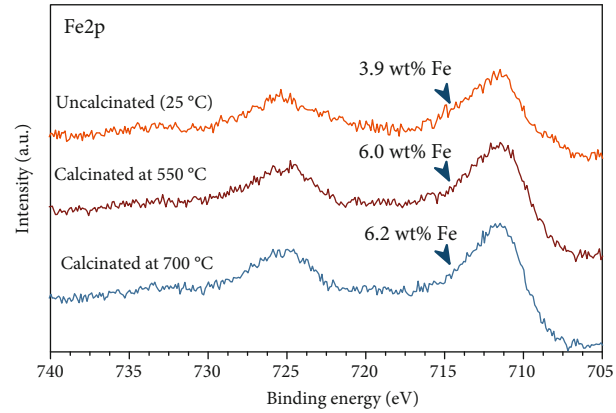

Figure 3: XPS spectra for Fe 2p of calcined and uncalcined MNZ/Fe surface.

units. These results demonstrated that composition could have variations because of the mineral nature [23]. This was in agreement with the previous work reported by Domenzain et al. [23]. On that research, the composition of Fe in a MNZ without impregnation was about 2.3 w% identified by EDS analyses and 2.6 w% of Fe oxides quantified by atomic absorption.

Fe can be present in natural minerals as different species, one of the most common is the magnetite (Fe_3O_4), which is a compound of mixed valence and commonly expressed with the notation as $(Fe^{3+})_{tet}(Fe^{2+}Fe^{3+})_{oct}O_4$. Due to rapid jump of electrons which move with a frequency of approximately 10^{-11} s at room temperature, the octahedral ions Fe^{3+} and Fe^{2+} can be written as $Fe^{2.5+}$ [24]. In addition, the Mössbauer spectrum of Fe_3O_4 at room temperature shows only two overlapping sextets which correspond to tetrahedral ions of Fe^{3+} and octahedral ions of $Fe^{2.5+}$.

XPS spectra of Fe species for uncalcined MNZ/Fe at 25°C and calcined MNZ/Fe at 550 and 700°C are shown in Figure 3. These were located between 705 and 740 eV of binding energy. Intensity variations in spectra were observed between calcined and uncalcined samples. The first one contained 3.9 w% of Fe on its surface, whereas the calcined samples (550 and 700°C) had 6 w% and 6.2 w% of Fe, respectively. The Fe spectrum has two representative peaks of Fe^{3+} ion characteristics of Fe_3O_4 structure, the main corresponds to Fe $2p_{3/2}$ located around 711.48 ± 0.2 eV [25] and the second peak is referred to as $2p_{1/2}$ situated in 724.60 ± 0.2 eV. These variations in Fe composition may be attributed to the following aspects: (1) the increase of Fe particles caused by impregnation, (2) the presence of other compounds on material surface that did not allow observing the Fe ions, (3) the change on the mineral structure due to the zeolitic species collapse after calcination, and (d) the amount of each compound varied depending on the analyzed crystal [23].

XPS spectrum of Fe at the core level is depicted in Figure 4, ranging from 705 to 740 eV. A characteristic model represented the two main signals of Fe $2p_{3/2}$ and Fe $2p_{1/2}$ with binding energies of $\sim 711.48 \pm 0.2$ and $\sim 724.60 \pm 0.2$ eV which appeared to correspond to iron oxide Fe^{3+} in Fe_3O_4 (magnetite) phase [26, 27]. Two signals presented at $\sim 719.08 \pm 0.2$ and $\sim 732.68 \pm 0.2$ eV [28] are assigned to

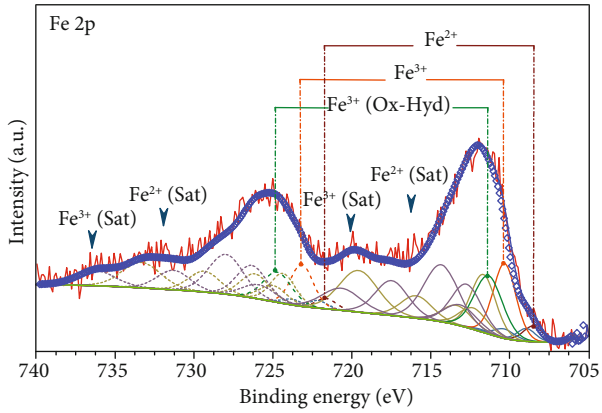

Figure 4: XPS spectrum at core level of MNZ/Fe in the Fe 2p region.

Table 2: XPS spectrum parameters at core level of Fe $2p_{3/2}$ for magnetite.

Specie	Chemical	Peak 1 (eV)	Peak 2 (eV)	Peak 3 (eV)
Magnetite	$Fe_3O_4\ (Fe^{2+})$	708.30 [a]	709.30 [b]	710.40 [b]
	$Fe_3O_4\ (Fe^{3+})$	711.30 [b]	712.40 [c]	713.60 [c]

[a] Refs. [27, 28, 32, 33], [b] Refs. [25, 27], [c] Ref. [25].

reorganization satellites. These are generally described as intrinsic energy losses that take place when the photoelectron leaves the atom in transition metals, such as Fe in metallic form or oxides. These signals showed reorganization characteristics at the core level that corresponded to the 2p energy level. In addition, the position of satellites is very sensitive to oxidation states of iron [29].

A satellite is an XPS signal of a photon that loses a small amount of energy and appears with a binding energy greater than the main peak. These signals of vibration at core level are caused by an X-ray photon that delivers a portion of its energy to the excitation of a secondary electron instead of giving the total amount of energy to a primary electron [29]. Fe compounds with oxidation state (II) had a shoulder in the photoelectric peak $2p_{3/2}$ corresponding to its satellite, while the satellite signal in oxidation state (III) was very characteristic, as shown in Figure 4 at ~720.38 ± 0.2 eV. On Fe species with mixed oxidation states (Fe^{2+}, Fe^{3+}), as is the case of Fe_3O_4, the satellite of charge transfer disappeared from the spectrum [30, 31]. Also, multiplets of Fe^{2+} and Fe^{3+} oxidation states for Fe_3O_4 species were observed in the $2p_{3/2}$ signal. These are presented in Table 2, where the main peaks of magnetite in its oxidation states, Fe^{3+} had a main peak at ~711.48 ± 0.2 eV, while Fe^{2+} species were found at ~708.58 ± 0.2 eV.

Fe species exposed on MNZ/Fe surface are reported in Table 3 for calcined and uncalcined samples. The uncalcined sample contained 43.9 w% of Fe^{3+} as oxide, 39.7 w% of Fe^{3+} as oxyhydroxides, and 16.4 w% of Fe^{2+} as oxide. With regard to calcined samples at 550 and 700°C, the amount of Fe^{3+}, oxide, and oxyhydroxide increased due to oxidation of Fe^{2+} to Fe^{3+} [34, 35]. After calcination at 550°C, the amount of Fe^{3+} as oxide increased to 45.7 w%, the same occurred for

Table 3: Fe species on the MNZ/Fe surface.

Species	Composition (w%)		
	Uncalcined	550°C	700°C
Fe2p3, Fe^{3+} (oxide)	43.90	45.70	46.60
Fe2p3, Fe^{3+} (oxyhydroxides)	39.70	41.40	42.20
Fe2p3, Fe^{2+} (oxide)	16.40	12.90	11.20

oxyhydroxides which increased to 41.4 w%, but Fe^{2+} decreased to 12.9 w%. Evenly, for calcined sample at 700°C, the oxides increased up to 46.6 w%, oxyhydroxides up to 42.2 w%, and Fe^{2+} oxides decreased to 11.2 w%. This could be explained because a part of the Fe^{2+} was oxidized to Fe^{3+}; however, the signals of magnetite and oxyhydroxides were only observed.

3.3. Mössbauer and Raman Spectroscopy. The Mössbauer spectra of uncalcined and calcined MNZ/Fe are shown in Figure 5. The spectra were recorded at 27°C, the adsorption spectra were adjusted with program NORMOS [36], the γ radiation source was 57Co of 925 MBq (25 mCi) inside a rhodium matrix, and the displacement of chemical isomer shift (δ) were given in relation with α-Fe. The observed signals in Figure 5(a) corresponded to Fe^{2+} and Fe^{3+} ions. Both were in a proportion of 45.5 w% and 54.5 w%, in that order. These signals are called doublets and are generally present in species that contain magnetic iron [37]. Based on the parameters of Mössbauer doublets, the Fe^{2+} fraction was related to fayalite species $(Fe^{2+})_2SiO_4$ with a chemical isomer shift of 1.13 mm/s [38]. These species belonged to nesosilicates class commonly found in volcanic rocks, and Fe^{3+} fraction were associated to magnetite species with a $\delta = 0.24$ mm/s [39] as listed in Table 4. The spectrum showed in Figure 5(b) for the MNZ/Fe calcined sample at 700°C presented 15.7% of relative area which corresponded to Fe^{2+}. Two more peaks were identified as Fe^{3+} with 13% and 71.3%. The doublet of Fe^{2+} agreed with magnetite species with a $\delta = 0.63$ mm/s [40], as well as the second signal of Fe^{3+} that also coincided with magnetite ($\delta = 0.29$ mm/s) [39–41]. The changes in Fe^{3+} quantity may be due to (a) oxidation process from Fe^{2+} to Fe^{3+} caused by MNZ/Fe calcination or (b) heterogeneous nature of mineral that can vary its composition of both Fe and zeolite species. The doublet of Fe^{3+} species that had a relative area of 13% presented a $\delta = 0.11$ mm/s, which was a characteristic of chlorite species [42, 43], this Fe specie was a crystalline aluminosilicate associated to the phyllosilicates group with a condensed chemical formula of $(Fe)_3(Si,Al)_4O_{10}(OH)_2(Fe)_3(OH)_6$.

Additionally, Raman analyses are shown in Figure 6. Based on Figure 6(a), a black Fe cluster with an irregular shape and 13.5 μm of diameter was impregnated on the zeolite matrix. This was corroborated with micro-Raman spectrum in Figure 6(b) where signals were presented in lengths of 193, 219, 346, 630, and 668 cm^{-1} related to magnetite species [44, 45]. Therefore, the acid solution during the impregnation process allowed Fe clustering to be embedded

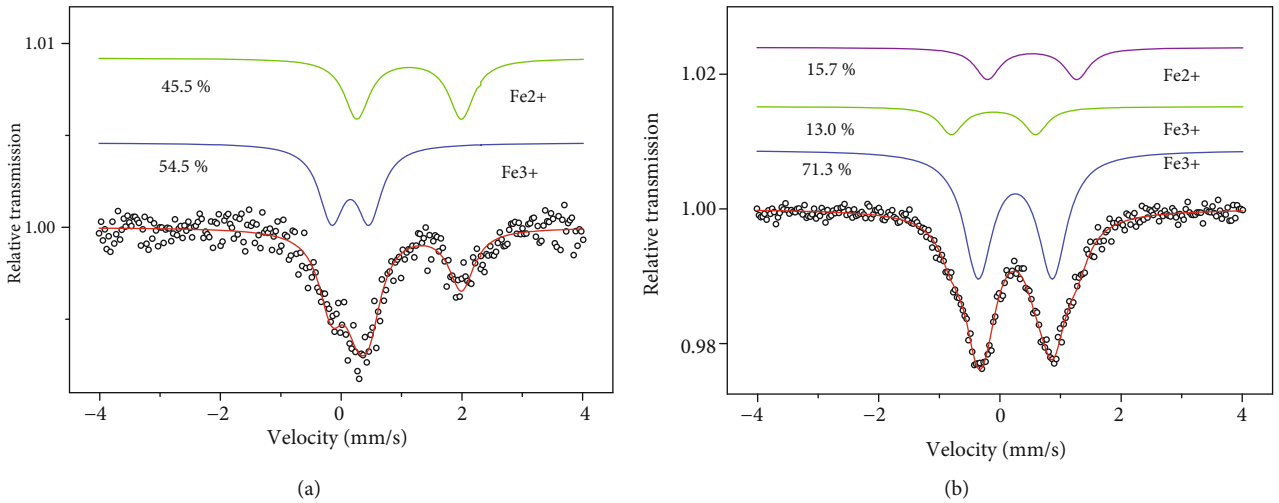

Figure 5: Mössbauer spectra of MNZ/Fe: (a) uncalcined at 25°C and (b) calcined at 700°C.

Table 4: Mossbauer parameters of MNZ/Fe samples.

Sample	δ (mm/s)	Δ (mm/s)	Γ (mm/s)	Fe	Relative area (%)
Uncalcined MNZ/Fe	1.13	1.73	0.51	Fe^{2+}	45.5
	0.24	0.62	0.51	Fe^{3+}	54.5
Calcined MNZ/Fe at 700°C	0.63	1.47	0.50	Fe^{2+}	15.7
	0.11	1.39	0.50	Fe^{3+}	13.0
	0.29	1.22	0.50	Fe^{3+}	71.3

δ = isomer shift relative to α-Fe at room temperature; Δ = quadrupole splitting; Γ = line width.

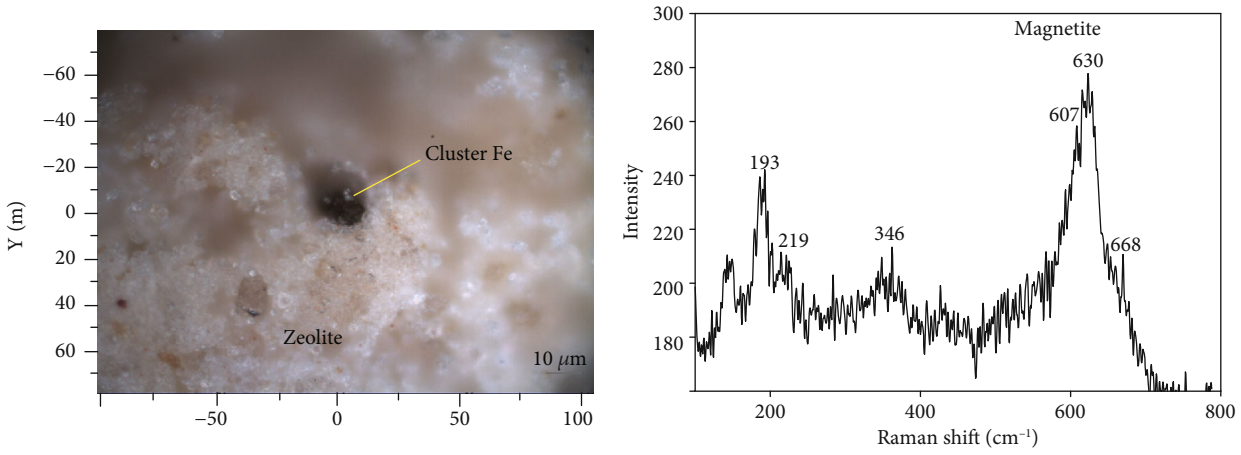

Figure 6: Raman spectrum for MNZ/Fe calcined at 700°C: (a) optic image and (b) micro-Raman spectrum.

on the mineral surface since the natural zeolite has a negative Z potential at these conditions [7].

3.4. Transmission Electron Microscopy (TEM). The structure and morphology of MNZ impregnated with Fe was attained by TEM analyses and the images were processed through the Digital Micrograph (Gatan Program, version 3.30.2016.0). Each image was calibrated in nanometer scale, later the Fast Fourier Transform (FFT), and finally the inverse FFT were applied to obtain lattice distance for each sample. TEM images depicted in Figure 7 belong to uncalcined MNZ/Fe samples.

The MNZ matrix can be observed at a scale of 100 nm from Figure 7(a) where the embedded Fe particles have a size of ~8.32 nm, meanwhile an irregular Fe particle was observed in Figure 7(b) with a size of 6.62 nm. In addition, the lattice distance was estimated to be 0.253 nm and the plane (311) is characteristic of crystalline magnetite (Fe_3O_4) nanoparticles

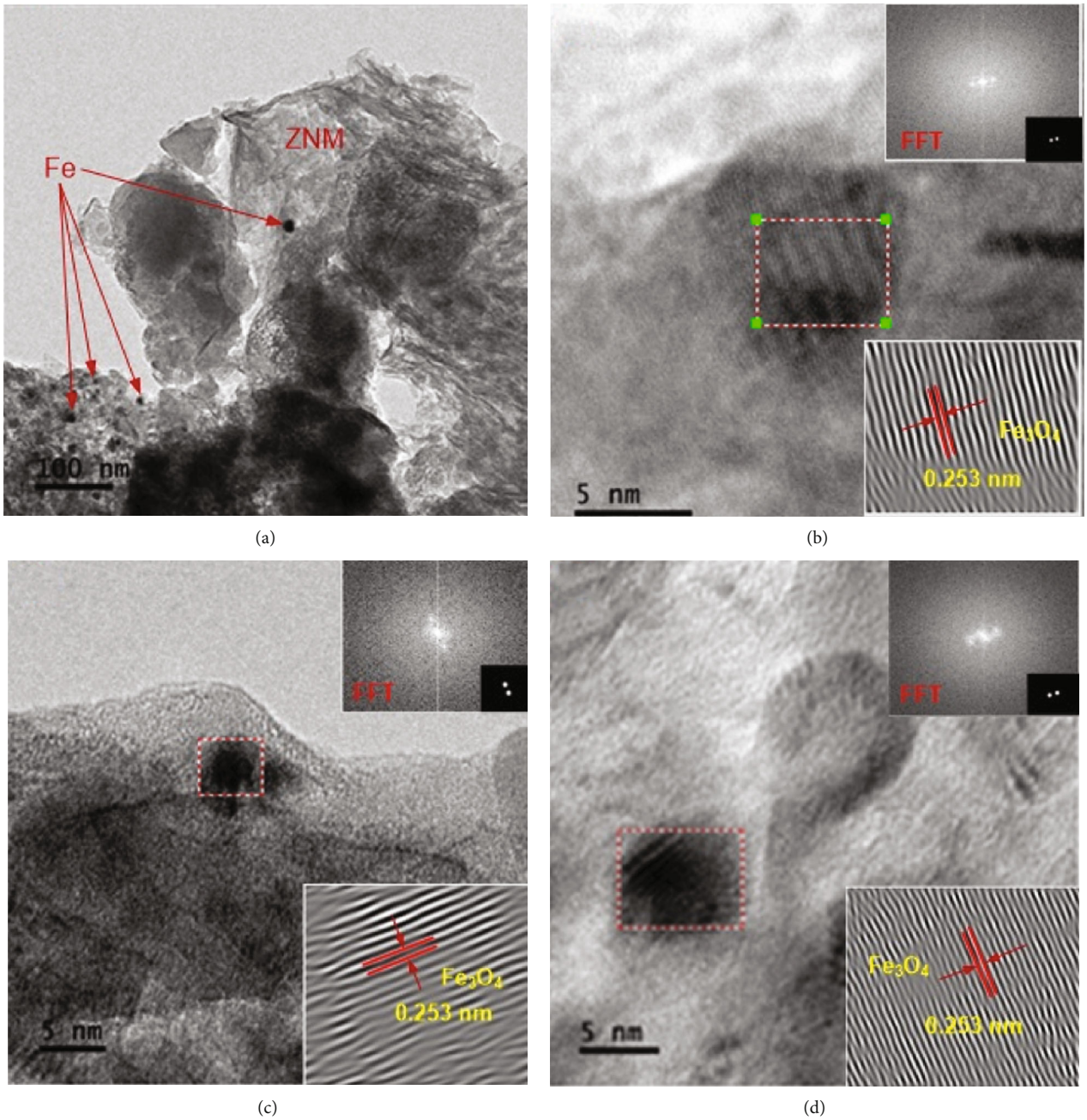

Figure 7: TEM images of uncalcined MNZ/Fe: (a) scale of 100 nm, (b-d) scale of 5 nm.

[46]. Based on Figures 7(c) and 7(d) scaled at 5 nm, the spacing of 0.253 nm and a plane of (311) confirmed the presence of magnetite species where Fe particles were found with sizes of 3.89 and 5.67 nm, respectively.

Similarly, TEM images of calcined MNZ/Fe samples at 700°C are depicted in Figure 8. The zeolite support was observed in Figure 8(a) with irregular incrustations of Fe particles up to 1 nm. The FTT patterns included in Figures 8(b) and 8(c) demonstrated that the lattice distance was 0.49 nm with a plane (111) [47]. This evidence denoted that the crystalline magnetite species were still present after calcination process, and Fe_3O_4 particles had a size of 19.63 nm (b) and 12.46 nm (c).

4. Catalytic Evaluation of MNZ/Fe

Reactive Black 5 (RB5) dye degradation in aqueous solutions was carried out by photo-Fenton heterogeneous process in order to evaluate the catalytic activity of the MNZ impregnated with Fe particles as a catalyst. This kind of metal can promote formation of hydroxyl radicals from peroxide [48–53] and Fe is more feasible to be impregnated by economic and environmental friendly method.

Fenton process consists of reaction of Fe^{2+} with hydrogen peroxide under acid conditions for production of hydroxyl radicals ($OH^{\cdot}$), which is highly reactive [54, 55]. The oxidation mechanism Fe^{2+} with H_2O_2 consists of transferring an

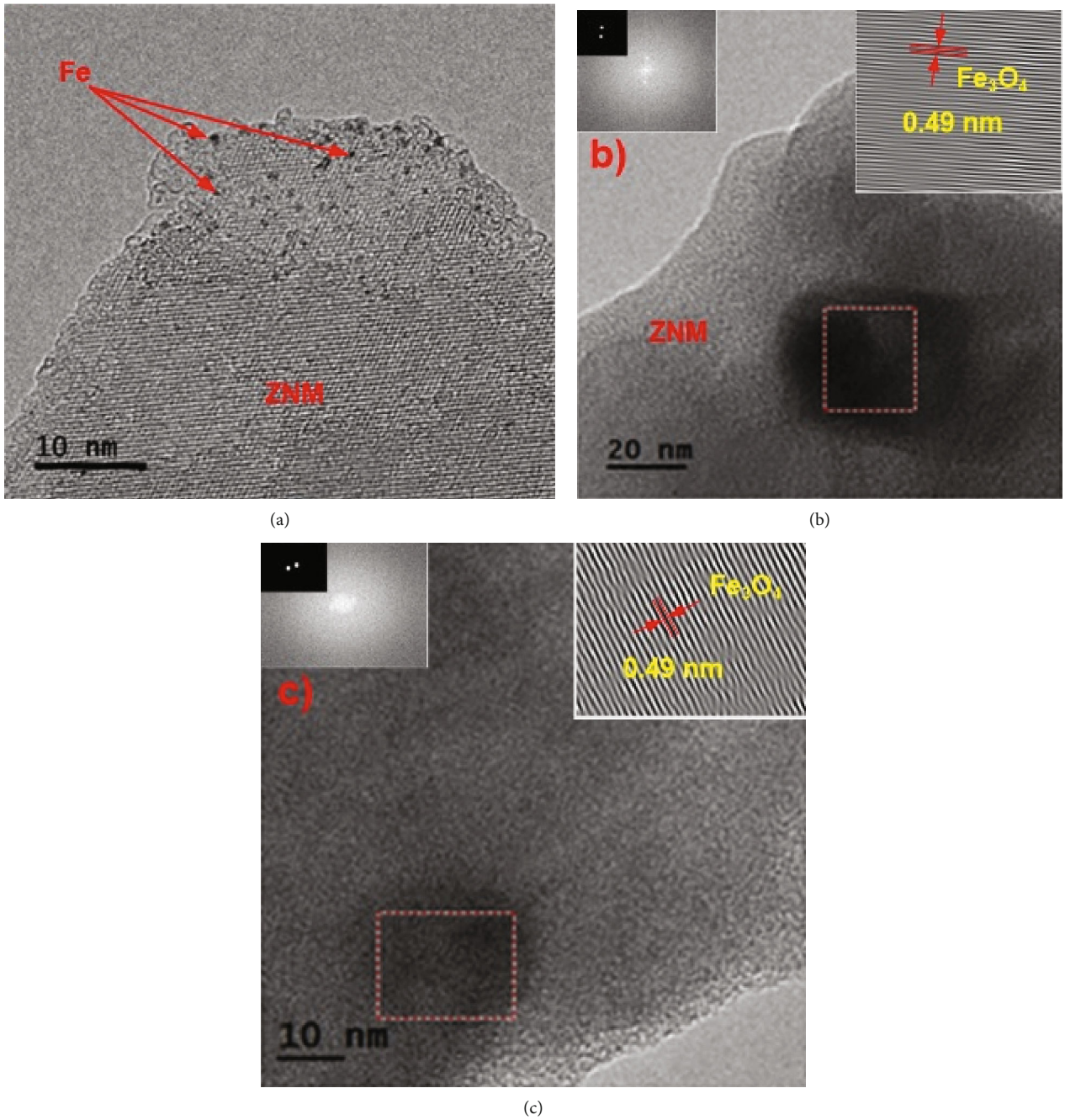

Figure 8: TEM images of calcined MNZ/Fe at 700°C: (a) scale of 10 nm, (b) scale of 20 nm, and (c) scale of 10 nm.

electron from the valence shell to the hydroxyl radicals and hydroxyl anions (reaction 1) [55, 56]. Other reactions associated with Fenton process are shown in reactions 2–7, which can occur simultaneously [57, 58]. These reactions are reached so quickly and are considered undesirable since hydroxyl radicals are not produced and hence an inhibition of Fenton reaction.

$$Fe^{2+} + H_2O_2 \longrightarrow Fe^{3+} + OH^- + OH^{\bullet} \quad (1)$$

$$Fe^{3+} + H_2O_2 \longleftrightarrow Fe - OOH^{2+} + H^+ \quad (2)$$

$$Fe - OOH^{2+} \longrightarrow OOH\cdot + Fe^{2+} \quad (3)$$

$$Fe^{2+} + OH\cdot \longrightarrow Fe^{3+} + OH^- \quad (4)$$

$$H_2O_2 + OH\cdot \longrightarrow H_2O + OOH\cdot \quad (5)$$

$$Fe^{3+} + OOH\cdot \longrightarrow Fe^{2+} + O_2 + H^+ \quad (6)$$

$$Fe^{2+} + OOH\cdot \longrightarrow Fe^{3+} + OOH^- \quad (7)$$

A variant of this process is photo-Fenton reaction [59, 60] in which a photooxidation takes place through a radiation source of Fe^{3+} hydrated followed by a transfer of photo-induced electrons where Fe^{2+} and $OH^{\cdot}$ are formed, as shown

Table 5: Catalytic evaluation conditions of MNZ impregnated with $FeCl_3$.

Reaction	Calcination temperature (°C)	(MNZ/Fe) (g/L)	MNZ/Fe (mg/g)
MNZ 1	Uncalcined	0.05	—
MNZ 2	Uncalcined	0.05	10
MNZ 3	550	0.05	5
MNZ 4	550	0.05	10
MNZ 5	700	0.05	5
MNZ 6	700	0.05	10

pH = 2.5; H2O2 = 3 g/L; (RB5)0 = 100 mg/L; λ = 405 nm.

in equations (8) and (9).

$$Fe^{3+} + H_2O \rightarrow Fe(OH)^{2+} + H^+ \quad (8)$$

$$Fe(OH)^{2+} + h\nu \rightarrow Fe^{2+} + OH\bullet \quad (9)$$

Finally, the main reaction for the present work between the RB5 dye and hydroxyl ions is presented in equation (10). The preferable products are carbon dioxide and water, but low-molecular-weight compounds could be obtained as secondary products when complete degradation is not achieved.

$$OH\cdot + RB5 \rightarrow \text{lowmolecularweight compounds} + CO_2 + H_2O \quad (10)$$

4.1. Calcination Temperature Effect and Fe Amount. Calcination temperature effect over MNZ impregnated with 5 and 10 mg MNZ/Fe was evaluated for RB5 dye degradation by means of photo-Fenton process. Calcined and uncalcined MNZ/Fe samples were used in different reactions as tabulated in Table 5. This evaluation was carried out at initial conditions of pH = 2.5, H_2O_2 = 3 g/L, $(RB5)_0$ = 100 mg/L, solution of (MNZ/Fe) = 0.05 g/L, and a radiation source of 405 nm (2.2 W). These conditions were used to avoid shielding and deactivation effects due to catalyst amount in the solution.

The UV-Vis absorption spectrum of $(RB5)_0$ dye at 100 mg/L and its degradation process is observed in Figure 9 ranged each 10 min. Its chromophore signal (597 nm) was the unique one taken into account because it is the most representative. This signal decreases gradually, while the absorbance on the signals at 312 and 392 nm was observed to increase at the beginning of the reaction, but these diminished after 10 min. The absorbance increase in the first 10 minutes could be due to the fact that lower molecular weight compounds were being produced during the RB5 dye removal. These other compound absorbed these wavelengths (392 nm and 312 nm) making it difficult to analyze the signals.

The kinetics for the RB5 dye discoloration at the conditions described in Table 5 is observed in Figure 10.

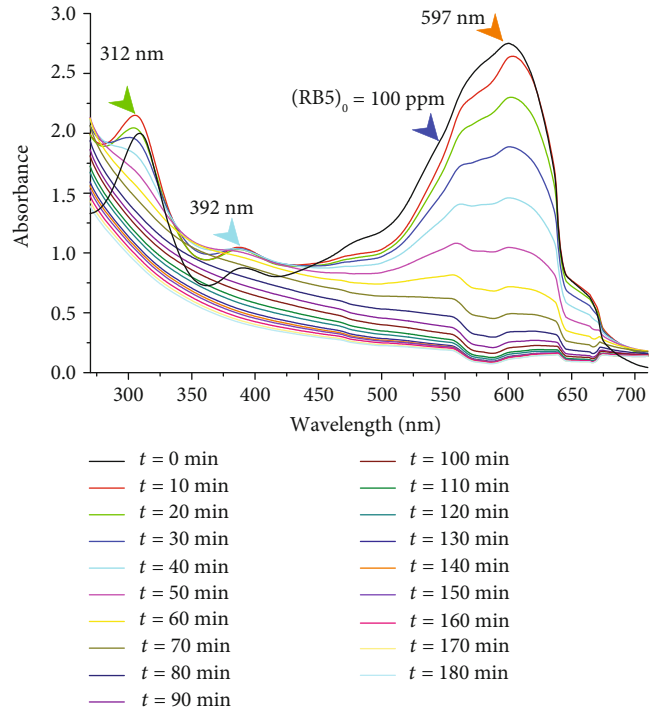

Figure 9: UV-Vis spectra of RB5 dye degradation by heterogeneous photo-Fenton process using MNZ/Fe.

In all cases, the discoloration percentage (D_t%) was calculated using equation (11) [61]:

$$D_t\% = \frac{C_0 - C_t}{C_0} \times 100 \quad (11)$$

Where C_0 is referred to as the initial concentration of RB5 dye and C_t denotes the corresponding concentration at a certain time. The MNZ 1 reaction was evaluated using a natural zeolite without Fe impregnated and without radiation source; it can be seen that there was no decrease in RB5 discoloration at these conditions and there was not adsorption of dye in the zeolite matrix, because the UV-Vis spectrum signal of the RB5 dye had not any changes during the process. The reactions MNZ 2, MNZ 3, MNZ 4, MNZ 5, and MNZ 6 were exposed to radiation by LED lamps in order to increase the production of $OH^{\cdot}$ radicals and thus form a greater quantity of hydroxyl ions. A slight decrease in coloration, only 6.5 D_{180}%, was obtained for the MNZ 2 reaction using uncalcined zeolite and impregnated with 10 mg MNZFe. A significant influence of the calcination temperature thought the reaction MNZ 3 produced a discoloration in the order of 25.2 D_{180}%.

Subsequently, a great activity was achieved for the first ten minutes of MNZ 4 reaction with 20 D_{10}% in RB5 dye discoloration. However, the activity only reached about 71.5 D_{180}% at the end of the reaction. This effect could be due to abrupt H_2O_2 consumption after the first ten minutes causing the intervention of hydroxyl ions in secondary reactions that did not degrade RB5 dye [62]. Reaction MNZ 5 produced a gradual discoloration reaching 79.42 D_{180}%. A similar

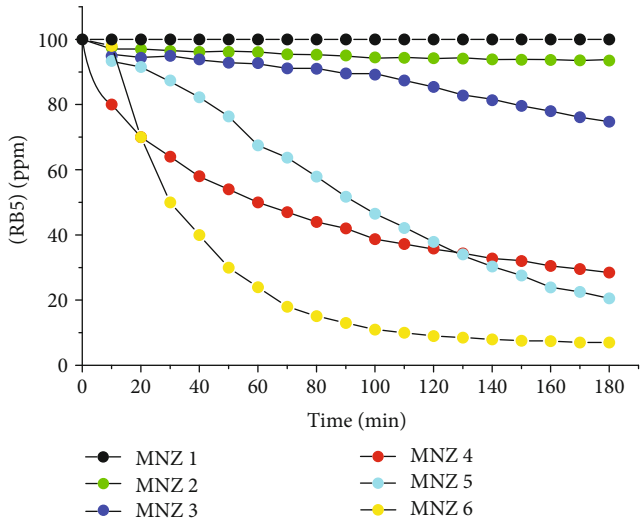

Figure 10: RB5 dye discoloration by heterogeneous photo-Fenton process using MNZ/Fe.

behavior was found in reaction MNZ 6 where a discoloration of 91 D_{180}% was achieved, been the maximum. The effect observed in the last two reactions could be due to the amount of Fe^{2+} and Fe^{3+} ions exposed on the MNZ surface, which benefited the interaction of these species with peroxide and light. Therefore, a greater $OH^{\cdot}$ ion formation was promoted and improved the photocatalytic activity in solution. In addition, the increase of Fe^{3+} concentration as oxide and oxyhydroxides compounds (magnetite and chlorite) also improved the catalytic activity [63].

About the kinetics of photocatalytic degradation, the Langmuir–Hinshelwood (L-H) model was utilized to describe the RB5 dye degradation [64–66]. It is expressed as follows:

$$r = -\frac{dC}{dt} = k_{app} C_t^n \quad (12)$$

where r is degradation rate, C_t refers to the concentration at a reaction time t, and k_{app} is the apparent rate constant, which includes L-H rate constant (k_{L-H}), and the adsorption constant (k_{ad}) [64–66], and the superscript n denotes the reaction order.

Different modifications to the L-H model are described elsewhere. Dong et al. [67] assumes that adsorption is a fast process and the determining stage for rate constant is the reaction that involves the species present in a monolayer of the solid-liquid interface. Therefore, the final expression for pseudo-first-order reactions is as follows:

$$\ln\left(\frac{C_0}{C}\right) = k_{app} t \quad (13)$$

In this work, equation (13) was used for the evaluation of the apparent rate constant and its values are presented in Table 6.

Table 6: Apparent rate constant of RB5 dye degradation.

Reaction	k_{app} (min^{-1})	R^2
MNZ 1	—	—
MNZ 2	0.0005	0.92
MNZ 3	0.0015	0.94
MNZ 4	0.0080	0.94
MNZ 5	0.0083	0.91
MNZ 6	0.0089	0.96

Table 7: RB5 dye discoloration using MNZ/Fe as catalyst.

MNZ/Fe (10 mg $FeCl_3$/g MNZ) @ 700°C				
Reaction	(MNZ/Fe) (g/L)	D_{180}%	k_{app} (min^{-1})	R^2
MNZ 6	0.05	91	0.0089	0.96
MNZ 7	0.10	92	0.0156	0.96
MNZ 8	0.15	92	0.0207	0.92
MNZ 9	0.20	93	0.0225	0.97
MNZ 10	0.35	91	0.0129	0.96
MNZ 11	0.50	86	*0.04200	0.90
MNZ 12	1.00	79	**0.044700	0.87
MNZ 13	1.50	29	0.0019	0.98

*k_{app} determined at 50 min; **k_{app} determined at 30 min.

k_{app} was obtained from RB5 concentration and reaction time by means of the linearization of time against ln (C_0/C). It is noted that $k_{app} = 0$ for MNZ 1 reaction because there was a not catalytic activity, meanwhile the highest activity was obtained for MNZ 6 reaction with a $k_{app} = 0.0089$ min^{-1} with a correlation coefficient $R^2 = 0.96$.

4.2. Catalyst Dosage Effect. The chemical reactions can improve dye degradations according to the influence of each variable. The best RB5 dye degradation was attained with 10 mg MNZ/Fe calcined at 700°C. Based on these material specifications, the catalyst (MNZ/Fe) dosage effect in solution was analyzed for optimization purposes and avoiding shielding and inhibition effects caused by the catalyst concentration. The reaction conditions from MNZ 6 to MNZ 13 are presented in Table 7. The catalyst dosage effect was observed by keeping constant pH = 2.5, $(H_2O_2) = 3$ g/L, $(RB5)_0 = 100$ mg/L, and lamp radiation $\lambda = 405$ nm (2.2 W).

The behavior of RB5 dye discoloration with respect to catalyst dosage in solution was measured at 180 min (D_{180}%) as illustrated in Figure 11. The discoloration percentage exceeded 90 D_{180}% at (MNZ/Fe) = 0.05 – 0.2 g/L where the optimum discoloration yielded 93 D_{180}% at 0.2 g/L on MNZ 9 reaction. On the other hand, the discoloration diminished as the (MNZ/Fe) was increasing. The D_{180}% decreases when using 0.35 g/L yielding 91. Consequently, the D_{180}% was decreasing with values of 86, 79 and 29 D_{180}% for catalyst dose of 0.5, 1, and 1.5 g/L, in that order. The low discoloration seemed to be attributed by the

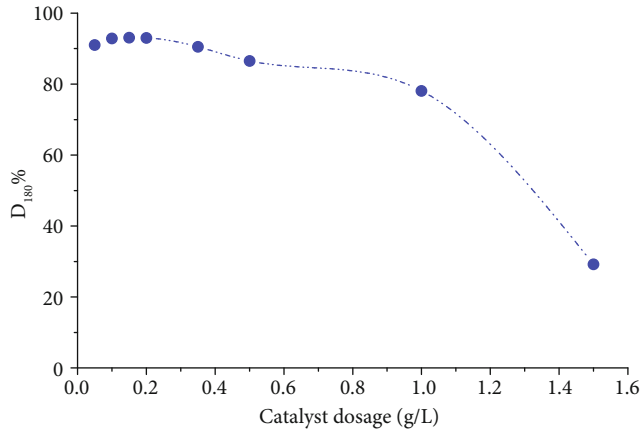

Figure 11: Catalyst dosage effect over RB5 dye discoloration at 180 min (D_{180}%).

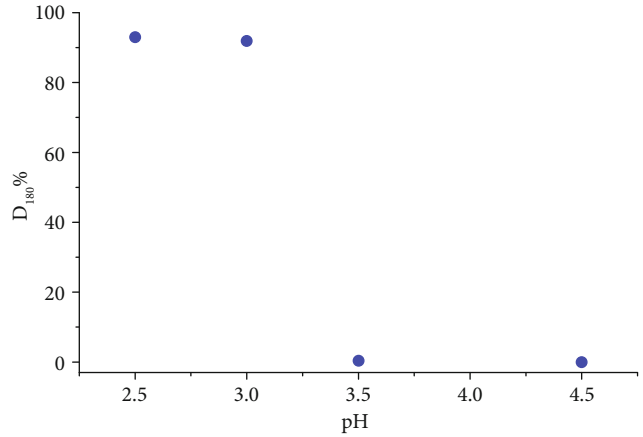

Figure 12: pH effect on RB5 dye discoloration using (MNZ/Fe) = 0.2 g/L as catalyst.

deactivation through shielding effect. It is caused by the MNZ opacity in solution where radiation and peroxide amount promoted a re-oxidation of Fe^{2+} ions [68].

The k_{app} values from MNZ 6 to MNZ 13 reactions are reported in Table 7 where pseudo-first-order was assumed for the reaction kinetics. The MNZ 9 reaction has the highest k_{app} after 180 min of reaction (0.0225 min^{-1}). The kinetic constant was evaluated at 50 and 30 min for MNZ 11 and MNZ 12 reactions, respectively. No apparent change in RB5 dye concentration was noted beyond these times.

4.3. pH Effect on the Solution. Heterogeneous materials have a high catalytic activity in Fenton process for dye degradation in a wide pH range [69]. Then, the pH dependence in RB5 dye discoloration was analyzed in the pH interval of 2.5–4.5 and keeping constant (MNZ/Fe) = 0.2 g/L, (H_2O_2) = 3 g/L, and $(RB5)_0$ = 100 mg/L.

The discoloration percentage RB5 dye after 180 min of reaction (D_{180}%) is observed in Figure 12 as a function of pH solution. A discoloration of 93 D_{180}% was obtained at pH = 2.5 and 91 D_{180}% at pH = 3. However, there was no dye discoloration when pH was increased between 3.5 and 4.5.

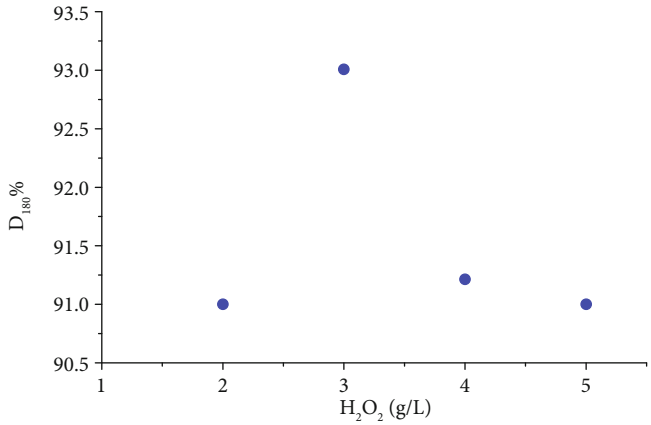

Figure 13: Effect of H_2O_2 concentration on RB5 dye degradation using (MNZ/Fe) = 0.2 g/L as catalyst.

4.4. Influence of H_2O_2 Concentration. The analysis of H_2O_2 concentration in the solution was carried out by keeping constant the amount of catalyst (MNZ/Fe) = 0.2 g/L, initial dye concentration $(RB5)_0$ = 100 mg/L, and a solution acidity pH = 2.5. Results depicted in Figure 13 demonstrated that using (H_2O_2) = 3 g/L, the major discoloration yielded 93 D_{180}% with a k_{app} = 0.0225 min^{-1}. Below and above this mentioned concentration, the discoloration seemed to be inhibited as reported by the decrease in the D_{180}% and the k_{app}. The values were 91 D_{180}% (k_{app} = 0.0131 min^{-1}), 91.2 D_{180}% k_{app} = 0.0153 min^{-1}), and 91 D_{180}% k_{app} = 0.0151 min^{-1}) for (H_2O_2) fixed at 2.0, 4.0, and 5.0 g/L, respectively. This was because increasing peroxide amount was likely to promote secondary reactions that consume H_2O_2 and therefore inhibit the RB5 degradation reaction.

4.5. Initial Concentration of RB5 Dye $(RB5)_0$. The initial concentration of RB5 dye was also studied by keeping constant the amount of H_2O_2 = 3 g/L, pH = 2.5, and catalyst (MNZ/Fe) = 0.2 g/L. Results are shown in Figure 14. In general, the great activity ocurred in the first reaction minutes. The major discoloration was obtained using $(RB5)_0$ = 100 mg/L on the MNZ 9 reaction with 89 D_{100}% at 100 min; later, the reaction tended to be slow since at 180 min reached 93 D_{180}%. For $(RB5)_0$ = 80 mg/L, the discoloration was gradual but with a slower reaction rate than the reported one by 100 mg/L. 61 D_{100}% was obtained and subsequently the reaction slowed down reaching 72 D_{180}% with a k_{app} = 0.0139 min^{-1} (R^2 = 0.96) at $(RB5)_0$ = 80 mg/L. In addition, a similar behavior like using 80 mg/L was exhibited when the initial concentration of RB5 was reduced to 60 and 40 mg/L. Discoloration yielded 40 D_{100}% and 51 D_{180}% with a k_{app} = 0.0113 min^{-1} (R^2 = 0.95) for $(RB5)_0$ = 60 mg/L. Subsequently, if $(RB5)_0$ = 40 mg/L were used, 26 D_{100}% and 34 D_{180}% k_{app} = 0.0113 min^{-1} (R^2 = 0.95) were obtained. The difference observed in D_t% was because on the $(RB5)_0$ decreased, and thus it made it difficult to achieve a suitable interaction between the $OH^{\cdot}$ radicals and the compounds to be removed.

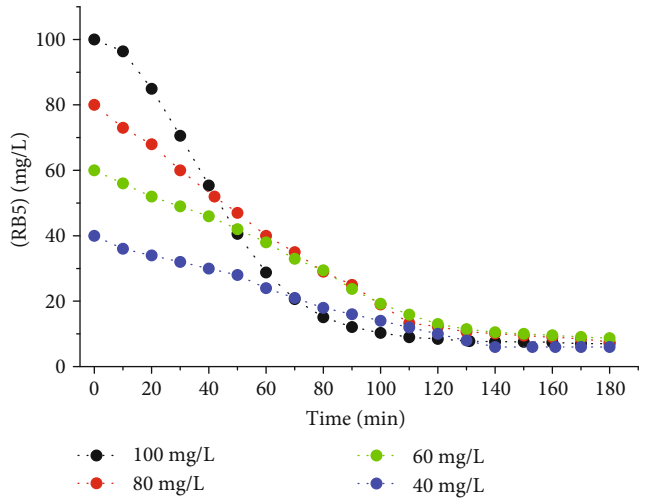

Figure 14: Effect of initial concentration of $(RB5)_0$ using (MNZ/Fe) = 0.2 g/L as catalyst.

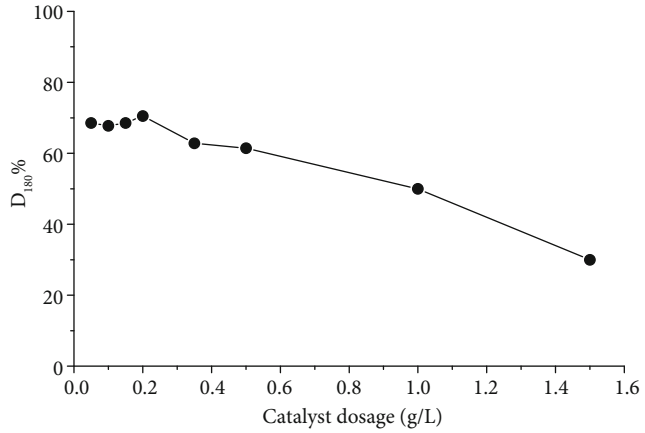

Figure 15: COD removal of RB5 dye.

4.6. COD Removal. The removal of $(RB5)_0 = 100$ mg/L using different concentrations of MNZ/Fe was determined at pH = 2.5, $(H_2O_2) = 3$ g/L, and light radiation (405 nm) for measuring chemical oxygen demand (COD) removal. The COD removal percentage after 180 min of reaction (COD_{180}%) is observed in Figure 15.

It was determined by equation (14):

$$COD_t\% = \frac{COD_0 - COD_t}{COD_0} \times 100 \quad (14)$$

The subscripts 0 and t denote the COD removal at initial and fixed time, respectively. The great COD removal was observed at concentrations of 0.05, 0.1, and 0.15 g/L (MNZ/Fe) with degradations of 68.5, 67.7, and 68.5 COD_{180}%, in that order. The highest removal (70.5 COD_{180}%) was achieved with (MNZ/Fe) = 0.2 g/L. The efficiency of the reaction was reduced when the catalyst concentration was increased to 0.35, 0.5, 1, and 1.5 g/L with corresponding removals of 62.8, 61.4, 50, and 30 COD_{180}%. This behavior was probably attributed to an increase on the catalyst amount that inhibited the reaction and the absence of active sites. Moreover, the opacity of the MNZ/Fe probably interfered with the reaction causing a shielding effect and therefore low interaction between the $OH^{\cdot}$ ions and the RB5 dye [68].

5. Conclusions

The Mexican natural zeolite (MNZ) studied in this research was constituted by heulandite, mordenite, erionite, and cristobalite phases, so the mineral was a mixture of crystalline aluminosilicates. The Fe composition on the MNZ surface as oxides and oxyhydroxides in the form of magnetite (Fe^{3+} and Fe^{2+}) was 3.9, 6 y 6.2 w% for samples uncalcined (25°C) and calcined at 550 and 700°C, respectively. Fe particles supported on the surface had sizes from 3.89 to 19.6 nm.

91 D_{180}% of discoloration was obtained for the 10 mg MNZ/Fe and calcined at 700°C. The reaction kinetics was assumed as pseudo-first order ($n = 1$). Besides, the D_{180}% decreased with catalyst dose increments, so that when using MNZ/Fe = 0.2 g/L the best discoloration (93 D_{180}%) was obtained. This photo-Fenton process had a positive effect on the RB5 discoloration at acidic conditions (pH = 2.5 and 3), achieving 93 D_{180}% (pH = 2.5). On the contrary, the reaction was inhibited at 3.5 and 4.5. Likewise, the amount of H_2O_2 and the initial concentration of RB5 dye were analyzed. The discoloration was more efficient with $(H_2O_2) = 3$ g/L. The reactions were slow after 120 min but the highest activity was achieved using $(RB5)_0 = 100$ mg/L. After 120 min, the $(RB5)_0$ did not represent an important variable, since there was no difference in the D_{180}%.

Finally, the highest COD removal was achieved at 180 minutes of reaction (70.5 COD_{180}%) using (MNZ/Fe) = 0.2 g/L. When the catalyst dose in aqueous solution increased to 1.5 g/L, the COD_{180}% was 30. This could be assumed that shielding effects or side reactions that consumed H_2O_2 were promoted, and hence the reaction efficiency decreased.

Data Availability

The data used to support the findings of this study are included within the article.

Conflicts of Interest

The authors declare no conflict of interest with respect to this publication.

Acknowledgments

The authors thank the Instituto Politécnico Nacional and CONACyT for the financial support, the Centro de Nanociencias y Micro y Nanotecnologias-IPN for the facilities to obtain the characterization of MNZ, and to Tobias N. Nava-Entzana for his assistance on Mössbauer analysis and Alfredo Pimentel-Rodas for his fruitful discussions.

References

[1] N. Das and P. Chandran, "Microbial degradation of petroleum hydrocarbon contaminants: an overview," *Biotechnology Research International*, vol. 2011, Article ID 941810, 13 pages, 2011.

[2] M. Alexander, "Biodegradation of organic chemicals," *Environmental Science & Technology*, vol. 19, no. 2, pp. 106–111, 1985.

[3] M. Wawrzkiewicz, M. Wisniewska, A. Wołowicz, V. M. Gun'ko, and V. I. Zarko, "Mixed silica-alumina oxide as sorbent for dyes and metal ions removal from aqueous solutions and wastewaters," *Microporous and Mesoporous Materials*, vol. 250, pp. 128–147, 2017.

[4] Z. Milán, E. Sánchez, P. Weiland, R. Borja, A. Martín, and K. Ilangovan, "Influence of different natural zeolite concentrations on the anaerobic digestion of piggery waste," *Bioresource Technology*, vol. 80, no. 1, pp. 37–43, 2001.

[5] R. Anand, T. Daniel, R. J. Lahoti, K. V. Srinivasan, and B. S. Rao, "Selective alkylation of phenol with cyclohexanol over large-pore zeolites," *Catalysis Letters*, vol. 81, no. 3-4, pp. 241–246, 2002.

[6] A. Corma and H. Garcia, "Zeolite-based photocatalysts," *Chemical Communications*, vol. 4, no. 13, pp. 1443–1459, 2004.

[7] G. Zacahua-Tlacuatl, J. Perez-Gonzalez, J. J. Castro-Arellano, and H. Balmori-Ramirez, "Rheological characterization and extrusion of suspensions of natural zeolites," *Applied Rheology*, vol. 20, no. 3, article 34037, 2009.

[8] M. Appl, *Ammonia*, Wiley, 2006.

[9] S. Erdal and M. Taskin, "Uptake of textile dye Reactive Black-5 by Penicillium chrysogenum MT-6 isolated from cement-contaminated soil," *African Journal of Microbiology Research*, vol. 4, no. 8, pp. 618–625, 2010.

[10] M. Perez-Moya, M. Graells, L. J. del Valle, E. Centelles, and H. D. Mansilla, "Fenton and photo-Fenton degradation of 2-chlorophenol: multivariate analysis and toxicity monitoring," *Catalysis Today*, vol. 124, no. 3-4, pp. 163–171, 2007.

[11] J. Hernandez and E. Meurer, "Óxidos de hierro en los suelos: sus propiedades y su caracterización con énfasis en los estudios de retención de fosforo," *Agrociencia*, vol. 1, no. 1, pp. 1–14, 1997.

[12] J. W. Stucki, B. A. Goodman, and U. Schwertmann, *Iron in soils and clay minerals*, Springer Nature, 1988.

[13] N. Kämpf and U. Schwertmann, "Goethite and hematite in a climosequence in southern Brazil and their application in classification of kaolinitic soils," *Geoderma*, vol. 29, no. 1, pp. 27–39, 1983.

[14] M. Lucas and J. Peres, "Decolorization of the azo dye Reactive Black 5 by Fenton and photo-Fenton oxidation," *Dyes and Pigments*, vol. 71, no. 3, pp. 236–244, 2006.

[15] E. Kusvuran, S. Irmak, H. Yavuz, A. Samil, and O. Erbatur, "Comparison of the treatment methods efficiency for decolorization and mineralization of Reactive Black 5 azo dye," *Journal of Hazardous Materials B*, vol. 119, no. 1-3, pp. 109–116, 2005.

[16] H. Sasaki, Y. Oumi, K. Itabashi, B. Lu, T. Teranishi, and T. Sano, "Direct hydrothermal synthesis and stabilization of high-silica mordenite (Si:Al = 25) using tetraethylammonium and fluoride ions," *Journal of Materials Chemistry*, vol. 13, no. 5, pp. 1173–1179, 2003.

[17] V. N. Smirenskaya and V. I. Vereshchagin, "Prospects of using zeolite rocks of Siberia in silicate materials," *Glass and Ceramics*, vol. 59, no. 11-12, pp. 414–419, 2002.

[18] D. L. Bish and D. W. Ming, "Natural zeolites: occurrence, properties, applications," *Mineralogical Society of America*, vol. 45, p. 654, 2001.

[19] P. Ballirano and G. Cametti, "Dehydration dynamics and thermal stability of erionite-K: Experimental evidence of the "internal ionic exchange" mechanism," *Microporous and Mesoporous Materials*, vol. 163, pp. 160–168, 2012.

[20] P. C. Yu, Y. W. Tsai, F. S. Yen, W. P. Yang, and C. L. Huang, "Thermal characteristic difference between α-Al_2O_3 and cristobalite powders during mullite synthesis induced by size reduction," *Journal of the European Ceramic Society*, vol. 35, no. 2, pp. 673–680, 2015.

[21] L. C. Castro, K. M. Degues, M. G. Cypriano, M. R. Rocha, O. R. K. Montedo, and E. Angioletto, "Evaluation of the thermal performance of different cold materials for urban paving," *Cerâmica*, vol. 63, no. 366, pp. 203–209, 2017.

[22] P. van der Heide, *X-Ray Photoelectron Spectroscopy: An Introduction to Principles and Practices*, John Wiley & Sons, First Edition edition, 2012.

[23] J. Domenzain, J. J. Castro, and L. A. Galicia, "Removal of RB5 dye using a Mexican natural zeolite: characterization and evaluation," *IJSER*, vol. 7, no. 9, 2016.

[24] B. Balko and G. R. Hoy, "Selective excitation double Mossbauer studies (SEDM) of electron hopping in magnetite (Fe_3O_4)," *Physica B+C*, vol. 86-88, pp. 953-954, 1977.

[25] A. P. Grosvenor, B. A. Kobe, M. C. Biesinger, and N. S. McIntyre, "Investigation of multiplet splitting of Fe 2p XPS spectra and bonding in iron compounds," *Surface and Interface Analysis*, vol. 36, no. 12, pp. 1564–1574, 2004.

[26] M. Mullet, V. Khare, and C. Ruby, "XPS study of Fe(II)-Fe(III) (oxy)hydroxycarbonate green rust compounds," *Surface and Interface Analysis*, vol. 40, no. 3-4, pp. 323–328, 2008.

[27] N. S. McIntyre and D. G. Zetaruk, "X-ray photoelectron spectroscopic studies of iron oxides," *Analytical Chemistry*, vol. 49, no. 11, pp. 1521–1529, 1977.

[28] M. Omran, T. Fabritius, A. M. Elmahdy, N. A. Abdel-Khalek, M. El-Aref, and A. E.-H. Elmanawi, "XPS and FTIR spectroscopic study on microwave treated high phosphorus iron ore," *Applied Surface Science*, vol. 345, pp. 127–140, 2015.

[29] P. Mills and J. L. Sullivan, "A study of the core level electrons in iron and its three oxides by means of X-ray photoelectron spectroscopy," *Journal of Physics D: Applied Physics*, vol. 16, no. 5, pp. 723–732, 1983.

[30] D. C. Frost, C. A. McDowell, and I. S. Woolsey, "X-ray photoelectron spectra of cobalt compounds," *Molecular Physics*, vol. 27, no. 6, pp. 1473–1489, 1974.

[31] D. C. Frost, A. Ishitani, and C. A. McDowell, "X-ray photoelectron spectroscopy of copper compounds," *Molecular Physics*, vol. 24, no. 4, pp. 861–877, 1972.

[32] A. R. Pratt, I. J. Muir, and H. W. Nesbitt, "X-ray photoelectron and Auger electron spectroscopic studies of pyrrhotite and mechanism of air oxidation," *Geochimica et Cosmochimica Acta*, vol. 58, no. 2, pp. 827–841, 1994.

[33] M. C. Biesinger, B. P. Payne, A. P. Grosvenor, L. W. M. Lau, A. R. Gerson, and R. S. C. Smart, "Resolving surface chemical states in XPS analysis of first row transition metals, oxides and

hydroxides: Cr, Mn, Fe, Co and Ni," *Applied Surface Science*, vol. 257, no. 7, pp. 2717–2730, 2011.

[34] D. C. Fernández-Remolar, "Iron oxyhydroxidesEncyclopedia of Astrobiology," pp. 855–857, 2011.

[35] J. L. Jambor and J. E. Dutrizac, "Occurrence and constitution of natural and synthetic ferrihydrite, a widespread iron oxyhydroxide," *Chemical Reviews*, vol. 98, no. 7, pp. 2549–2586, 1998.

[36] R. Brand, "Normos Mössbauer fitting program," *Nuclear INSTR and Meth B28*, vol. 398, 1987.

[37] E. S. Vasil'eva, O. V. Tolochko, V. G. Semenov, V. S. Volodin, and D. Kim, "Mössbauer spectroscopy analysis of the phase composition of iron-based nanoparticles," *Applied Physics Letters*, vol. 33, no. 1, pp. 40–43, 2007.

[38] F. B. Waanders and J. Nell, "Phase chemical composition of slag from a direct nickel flash furnace and associated slag cleaning furnace," *Hyperfine Interactions*, vol. 218, no. 1-3, pp. 101–105, 2013.

[39] M. d. F. F. Lelis, C. M. Gonçalves, J. D. Fabris, W. N. Mussel, and W. A. Pacheco Serrano, "Effectiveness of selective chemical treatments on concentrating magnetic minerals of samples from a nickel-ore peridotite mantle," *Journal of the Brazilian Chemical Society*, vol. 15, no. 6, pp. 884–889, 2004.

[40] S. Braccini, O. Pellegrinelli, and K. Krämer, "Mössbauer, X-ray and magnetic studies of black sand from the Italian Mediterranean Sea," *World Journal of Nuclear Science and Technology*, vol. 3, pp. 91–95, 2013.

[41] Y.-L. Li, S. M. Pfiffner, M. D. Dyar et al., "Degeneration of biogenic superparamagnetic magnetite," *Geobiology*, vol. 7, no. 1, pp. 25–34, 2009.

[42] J. R. Smyth, "Crystal structure refinement and Mössbauer spectroscopy of an ordered, triclinic clinochlore," *Clays and Clay Minerals*, vol. 45, no. 4, pp. 544–550, 1997.

[43] M. D. Dyar, D. G. Agresti, M. W. Schaefer, C. A. Grant, and E. C. Sklute, "Mössbauer spectroscopy of earth and planetary materials," *Annual Review of Earth and Planetary Sciences*, vol. 34, no. 1, pp. 83–125, 2006.

[44] L. V. Gasparov, D. Arenas, K.-Y. Choi et al., "Magnetite: Raman study of the high-pressure and low-temperature effects," *Journal of Applied Physics*, vol. 97, no. 10, p. 10A922, 2005.

[45] M. D. Dyar, D. G. Agresti, M. W. Schaefer, C. A. Grant, and E. C. Sklute, "Raman spectroscopy investigation of magnetite nanoparticles in ferrofluids," *Journal of Magnetism and Magnetic Materials*, vol. 322, no. 14, pp. 1904–1911, 2010.

[46] G. Li, R. Li, and W. Zhou, "A wire-shaped supercapacitor in micrometer size based on Fe_3O_4 nanosheet arrays on Fe wire," *Nano-Micro Letters*, vol. 9, no. 4, article 147, pp. 1–8, 2017.

[47] Y.-L. Chueh, M.-W. Lai, J.-Q. Liang, L.-J. Chou, and Z. L. Wang, "Systematic Study of the Growth of Aligned Arrays of α-Fe_2O_3 and Fe_3O_4 Nanowires by a Vapor–Solid Process," *Advanced Functional Materials*, vol. 16, no. 17, pp. 2243–2251, 2006.

[48] G. P. Anipsitakis and D. D. Dionysiou, "Radical generation by the interaction of transition metals with common oxidants," *Environmental Science & Technology*, vol. 38, no. 13, pp. 3705–3712, 2004.

[49] E. G. Heckert, S. Seal, and W. T. Self, "Fenton-like reaction catalyzed by the rare earth inner transition metal cerium," *Environmental Science & Technology*, vol. 42, no. 13, pp. 5014–5019, 2008.

[50] D. Mantzavinos, "Removal of benzoic acid derivatives from aqueous effluents by the catalytic decomposition of hydrogen peroxide," *Process Safety and Environmental Protection*, vol. 81, no. 2, Part B, pp. 99–106, 2003.

[51] R. J. Watts, J. Sarasa, F. J. Loge, and A. L. Teel, "Oxidative and reductive pathways in manganese-catalyzed Fenton's reactions," *Journal of Environmental Engineering*, vol. 131, no. 1, pp. 158–164, 2005.

[52] V. Shah, M. Bhatt, P. Stopka, and F. Nerud, "Copper based Fenton's system for the decolourization of synthetic dyes and dye industry effluents," *Asian Journal of Water, Environment and Pollution*, vol. 2, pp. 61–64, 2005.

[53] M. Falcon, K. Fajerwerg, J. N. Foussard, E. Puech-Costes, M. T. Maurette, and H. Debellefontaine, "Wet oxidation of carboxylic acids with hydrogen peroxide. Wet peroxide oxidation (WPO®) process. optimal ratios and role of Fe:Cu:Mn metals," *Environmental Technology*, vol. 16, no. 6, pp. 501–513, 1995.

[54] H. J. H. Fenton, "Oxidation of tartaric acid in presence of iron," *Journal of the Chemical Society*, vol. 65, pp. 899–910, 1894.

[55] F. Haber and J. Weiss, "The catalytic decomposition of hydrogen peroxide by iron salts," *Proceedings of the Royal Society of London. Series A - Mathematical and Physical Sciences*, vol. 147, no. 861, pp. 332–351, 1934.

[56] F. Haber and J. Weiss, "Über die Katalyse des Hydroperoxydes," *Naturwissenschaften*, vol. 20, no. 51, pp. 948–950, 1932.

[57] G. V. Buxton, C. L. Greenstock, W. P. Helman, and A. B. Ross, "Critical review of rate constants for reactions of hydrated electrons, hydrogen atoms and hydroxyl radicals $^{\bullet}OH/^{\bullet}O^{-}$ in aqueous solution," *Journal of Physical and Chemical Reference Data*, vol. 17, no. 2, pp. 513–886, 1988.

[58] T. Rigg, W. Taylor, and J. Weiss, "The rate constant of the reaction between hydrogen peroxide and ferrous ions," *The Journal of Chemical Physics*, vol. 22, no. 4, pp. 575–577, 1954.

[59] V. A. Nadtochenko and J. Kiwi, "Photolysis of $FeOH^{2+}$ and $FeCl^{2+}$ in aqueous solution. Photodissociation kinetics and quantum yields," *Inorganic Chemistry*, vol. 37, no. 20, pp. 5233–5238, 1998.

[60] R. G. Zepp, B. C. Faust, and J. Hoigne, "Hydroxyl radical formation in aqueous reactions (pH 3-8) of Iron (II) with hydrogen peroxide: the photo-Fenton reaction," *Environmental Science & Technology*, vol. 26, no. 2, pp. 313–319, 1992.

[61] B. Li, Y. Dong, Z. Ding, Y. Xu, and C. Zou, "Renovation and Reuse of Reactive Dyeing Effluent by a Novel Heterogeneous Fenton System Based on Metal Modified PTFE Fibrous Catalyst/H_2O_2," *International Journal of Photoenergy*, vol. 2013, Article ID 169493, 10 pages, 2013.

[62] S. Navalon, M. Alvaro, and H. Garcia, "Heterogeneous Fenton catalysts based on clays, silicas and zeolites," *Applied Catalysis B: Environmental*, vol. 99, no. 1–2, pp. 1–26, 2010.

[63] H. Zhan, Y. Bian, Q. Yuan, B. Ren, A. Hursthouse, and G. Zhu, "Preparation and potential applications of super paramagnetic nano-Fe_3O_4," *Processes*, vol. 6, no. 4, pp. 1–22, 2018.

[64] I. Kim and H. Tanaka, "Photodegradation characteristics of PPCPs in water with UV treatment," *Environment International*, vol. 35, no. 5, pp. 793–802, 2009.

[65] A. Piram, A. Salvador, C. Verne, B. Herbreteau, and R. Faure, "Photolysis of β-blockers in environmental waters," *Chemosphere*, vol. 73, no. 8, pp. 1265–1271, 2008.

[66] V. Romero, P. Marco, J. Giménez, and S. Esplugas, "Adsorption and Photocatalytic Decomposition of the β-Blocker

Metoprolol in Aqueous Titanium Dioxide Suspensions: Kinetics, Intermediates, and Degradation Pathways," *International Journal of Photoenergy*, vol. 2013, Article ID 138918, 10 pages, 2013.

[67] Y. Dong, W. Dong, Y. Cao, Z. Han, and Z. Ding, "Preparation and catalytic activity of Fe alginate gel beads for oxidative degradation of azo dyes under visible light irradiation," *Catalysis Today*, vol. 175, no. 1, pp. 346–355, 2011.

[68] F. Martínez, G. Calleja, J. A. Melero, and R. Molina, "Heterogeneous photo-Fenton degradation of phenolic aqueous solutions over iron-containing SBA-15 catalyst," *Applied Catalysis B: Environmental*, vol. 60, no. 3-4, pp. 181–190, 2005.

[69] A. C.-K. Yip, F. L.-Y. Lam, and X. Hu, "Novel bimetallic catalyst for the photo-assisted degradation of Acid Black 1 over a broad range of pH," *Chemical Engineering Science*, vol. 62, no. 18-20, pp. 5150–5153, 2007.